



Article

Rod-Shaped Carbon Aerogel-Assisted CdS Nanocomposite for the Removal of Methylene Blue Dye and Colorless Phenol

Saradh Prasad ^{1,2} , P. Shanmugam ³, K. Bhuvaneswari ⁴, G. Palanisamy ⁴, T. Pazhanivel ⁴, T. Arunkumar ⁵, Mohamed Saleh AlSalhi ^{1,2,*}  and Mamduh J. Aljaafreh ²

¹ Research Chair on Laser Diagnosis of Cancers, Department of Physics and Astronomy, College of Science, King Saud University, Riyadh 11451, Saudi Arabia; saradprasad@gmail.com

² Department of Physics and Astronomy, College of Science, King Saud University, Riyadh 11451, Saudi Arabia; maljaafreh@kus.edu.sa

³ Department of Chemistry, St. Joseph University, Dimapur, Nagaland 797115, India; shanmugachem@gmail.com

⁴ Smart Materials Interface Laboratory, Department of Physics, Periyar University, Salem-636 011, Tamilnadu, India; bhuviphy11@gmail.com (K.B.); saharapalani@gmail.com (G.P.); pazhanit@gmail.com (T.P.)

⁵ Department of Mechanical Engineering, CMR Institute of Technology, Bengaluru 560037, India; arunkumar.t@cmrit.ac.in

* Correspondence: malsalhi@ksu.edu.sa; Tel.: +966-50-510-4815

Received: 14 March 2020; Accepted: 11 April 2020; Published: 14 April 2020



Abstract: A carbon aerogel (CA)-assisted CdS nanocomposite was prepared by hydrothermal process and was investigated as a photocatalyst towards the photodegradation of methylene blue (MB) dye and colorless phenol under visible light irradiation (VLI). CdS have attracted wide attention due to their relatively narrow band gap for the visible light effect and the suitably negative potential of the conduction band (CB) edge for the neutralization of H⁺ ions. The obtained characterization results suggest that the CA-assisted CdS nanocomposite has enhanced photophysical properties, a more surface area, and the desired morphology at the nm scale. Under optimization, CdS CA 8% shows superior catalytic activity for degradation compared with other samples. The photocatalytic activities of the as-synthesized samples were examined under VLI through the MB and phenol degradation. Compared with pure CA and CdS, the CA (8%)-assisted CdS nanoparticles (NPs) offer significantly enhanced photocatalytic efficiency for MB and phenol. The mechanism of photocatalytic reaction was examined by adding various scavengers, and the results revealed that the holes generated in CA (8%)-assisted CdS NPs have a crucial impact on the visible light photocatalytic process. The improved photocatalytic degradation was due to the strong interaction between the CA and CdS NPs.

Keywords: carbon aerogel; cadmium sulfide; nanocomposite; dye degradation

1. Introduction

A diversity of organic dyes have been extensively utilized in different industries, such as the ink, ceramic, paper, cosmetics, textile, and food processing industries [1–3], and these wastewater cause environmental hazards to humans, microorganisms, and animals. The removal of pollutants from wastewater has concerned much consideration in recent years. Therefore, numerous efforts have been made to remove dyes from wastewaters, such as oxidation, carbon adsorption, photodegradation, biodegradation, electrolytic chemical treatment, chemical precipitation, and to processes membrane [4–6]. Among the various approaches, photocatalysis is an important process for the organic dyes removal in

aqueous media. Semiconductor based materials, such as TiO_2 , CdS, ZnS and ZnO, have been widely utilized for photocatalytic dye degradation [7–9]. Though, the photodegradation efficiency is limited by numerous factors, such as restrictive the absorption light to only UV light and the electrons (e^-) and holes (h^+) rapid recombination. Organic pollutants can be proficiently degraded via the creation of photoinduced electrons/holes under VLI. In commercial applications, semiconductor materials are hindered by their fundamental defects, such as a low quantum efficiency and the poor electronic properties of nanoparticles [10]. So, modifying a semiconductor with a narrow band gap can increase the photocatalytic behavior by utilizing high solar light, stimulating interfacial transfer of electron and decreasing recombination of charge [11–13].

In contrast, sulfide-related photocatalysts have received ample attention in contemporary years due to their outstanding VLI responses and outstanding photocatalytic performance [14,15]. In the past few decades, various metal sulfide-related photocatalysts have been reported for water splitting because the sulfides of transition metals have an appropriate conduction-band locus and an associated narrow band gap; hence, such compounds are used as visible light-responsive photocatalysts [16–18], in contrast to other semiconducting wide band gap materials that have played a prominent role in the photocatalytic process, especially cadmium sulfide (CdS) particles, which are prominent photocatalytic materials under visible light irradiation [19–21]. Generally, CdS is a direct band gap (2.4 eV) material that exhibits superior photophysical and photochemical properties. Hence, it can efficiently absorb visible light. CdS nanoparticles possess a sufficient conduction band edge and adequate negative reduction potential to replenish H^+ ions and retain a narrow band gap [22–24]. Nevertheless, there are some difficulties in using CdS, such as the limited light absorption and fast recombination of photoexcited charge carriers [25]. The improvement of the photocatalytic activity of CdS is a vital concern, so many research studies are focusing on improving the catalytic activity of CdS particles through their composition.

On the other hand, the incorporation and composition of CdS nanoparticles in carbon-based materials have received increasing interest [20,26,27]. CdS nanoparticles (NPs) are broadly employed as photoadsorbents due to their unique surface morphology and porosity. Therefore, many scientists have dedicated efforts to investigating new combinations of materials to enhance the nanostructure and porosity properties [19,28]. Xiubing Li et al. prepared a 3D porous aerogel with tungsten oxide nanowires, and the photocatalytic activities against organic dyes were investigated [29]. Similarly, Yuning Jin et al. also investigated TiO_2 /carbon aerogel as a catalyst for the removal of dye [30].

In light of the above ideas, we prepared carbon aerogel-assisted CdS photocatalysts with different weight percentages (1–8%) through a simple hydrothermal process. The photodegradation performance and the degradation mechanisms of the carbon aerogel (CA)-assisted CdS nanoparticles were examined against organic dye and colorless phenol under a visible photodegradation process. This work offers an active method for the treatment of wastewater to address environmental pollutants by using CA with CdS NPs.

2. Materials and Method

In this experiment, all the reagents and chemicals were attained from Shanghai Chemical Reagent Factory, China and utilized as such without additional purification.

2.1. Preparation of Carbonaceous Aerogel (CA)

The CA was synthesized by a simple hydrothermal technique, and a required amount of chitosan was dispersed in water. The homogeneous chitosan solution was kept in an autoclave and heated at 180 °C for 12 h. After natural cooling, to obtain a carbonaceous hydrogel, the as-obtained black CA was thoroughly rinsed with a 1:1 volume ratio ethanol:water mixture for the removal of impurities. The obtained hydrogel was treated by lyophilization for 36 h using a high-vacuum freeze-drying process at −50 °C.

2.2. Synthesis of CdS/CA

The Cadmium sulphide/carbon aerogel (CdS/CA) composites were produced by hydrothermal treatment. For instance, $\text{Cd}(\text{NO}_3)_2 \cdot 4\text{H}_2\text{O}$ (5 mmol) and thiourea (TU, 7.5 mmol) were dissolved in 0.05 L of ethylene glycol (EG) under sonication; then, 100 mg of CA was fully immersed into the above solution. The reaction mixture was placed in an autoclave and heated at 160 °C for 12 h. After cooling, the CdS/CA was thoroughly washed with an ethanol and water mixture to remove the impurities on the surface of the CdS/CA. Finally, CdS/CA was obtained by lyophilizing CdS/CA for 36 h using a high-vacuum freeze-drying process at −50 °C. A similar procedure was used to synthesize other composites, viz., 2, 4, 6 and 8 wt %.

2.3. Characterization Details

XRD studies of the as-prepared materials was accomplished on a Bruker AXS (Bruker, Karlsruhe, Germany) diffractometer with a diffraction 2θ range between 5° and 70°. The functional groups of the materials were inspected by FTIR spectroscopy using a Bruker Tensor 27. Raman spectrometry was used to examine the interatomic interactions of the prepared samples by using a Thermo Fisher DXR (USA) equipped with an HeNe laser. Absorption studies was performed by utilizing a UV–Vis–NIR spectrophotometer SHIMADZU 3600 (SHIMADZU, Kyoto, Japan). The surface structure and elemental mapping of the prepared material were inspected through SEM analysis by a Hitachi S-4800 (Hitachi, Chiyoda, Japan) and Horiba EMAX Energy EX-350 (Horiba, Kyoto, Japan), which were operated at 10 kV. The internal morphology of the CdS/CA composites was investigated through TEM analysis with the help of a JEOL-JEM-2010 (JEOL, Akishima, Tokyo, Japan).

2.4. Photocatalytic Reaction Test

The photocatalytic dye degradation ability of the prepared samples was studied by the degradation of aqueous MB dye under VLI. The reaction mixture was done by dispersing 0.25 g of photocatalyst in 0.1 L of MB dye solution containing an initial con. of 10 mg/L. Light was delivered by a xenon light of 500 W power, and prior to illumination, the photocatalyst and suspension of dye was mixed for 5 min and retained in a dark room for half hour to confirm desorption/adsorption equilibrium between MB and catalyst. After 30 min, 3 mL of the dye was removed by centrifugation to split the catalytic particles from the solution. After, the absorbance of the acquired supernatant dye concentration was measured by a UV–vis–NIR spectrophotometer UV-3600 (Shimadzu, Kyoto, Japan).

3. Results

Figure 1 displays the XRD patterns of CdS/CA samples with various weights. When increasing the concentration of CA, no noticeable variations were found in the XRD patterns. The diffraction patterns of the CdS are well matched to hexagonal CdS (JCPDS card no. 80-0006) [31]. The observed 2θ values for CdS are 25.6°, 23.9°, 27.2°, 35.48°, 42.15°, 46.36°, 50.6°, 50.9°, 56.32°, and 64.32°, which closely match the (100), (002), (101), (102), (110), (103), (200), (112), and (202) crystalline planes of the hexagonal of CdS, respectively. The absence of carbon peaks indicates a relatively low concentration of carbon aerogel, which did not disturb the CdS crystal structure [32]. The CA content in the CdS hybrid aerogels increased with weight ratio up to 8% CA.

The FTIR spectra of all the as-prepared materials are shown in Figure 2. The bands located between 3400 and 3600 cm^{-1} in all the spectra can be attributed to the stretching frequency of adsorbed H_2O [33]. Similarly, the peak at 1630 cm^{-1} can be attributed to the bending vibrations of adsorbed H_2O . The characteristic peaks at approximately 1650, 1400, and 1050 cm^{-1} may be attributed to the natural vibrations due to stretching of $\text{C}=\text{O}/\text{C}=\text{C}$, COO , and $\text{C}-\text{C}-\text{C}$, respectively [34]. The distinctive bands of absorption at 1115 and 1387 cm^{-1} are because of the Cd-S bonds stretching vibrations [35]. Likewise, the peaks below 1000 cm^{-1} represent the stretching modes of metal sulfides, which confirms the formation of M-S in the synthesis [36]. The M-S vibrations, and the C-C stretching vibrations, are

indication for the establishment of the CdS CA nanocomposite. The intensity of the absorption peak of CdS is decreased slightly upon enhancing the wt% of CA. The result of the FTIR analysis clearly showed the co-existence of the CdS and CA in the composite.

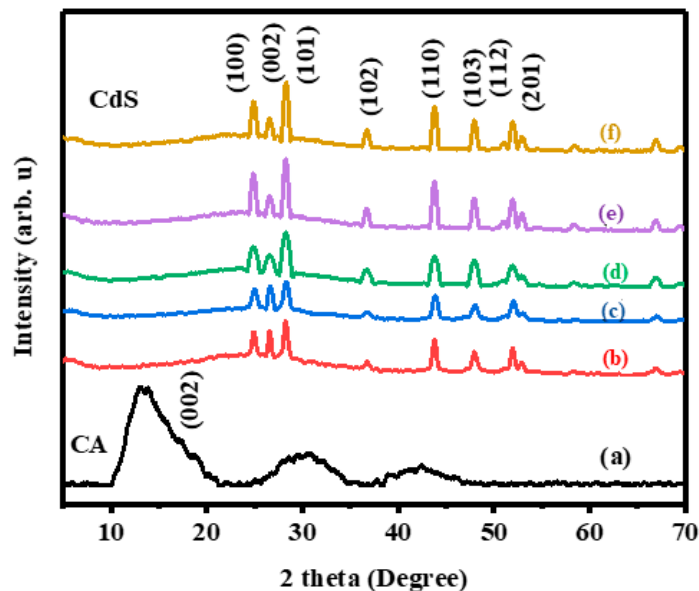


Figure 1. XRD patterns of (a) Pristine carbon aerogel (CA), (b) cadmium sulfide (CdS) 8%, (c) CdS CA 6% (d) CdS CA 4% (e) CdS CA 2% and (f) Pristine CdS.

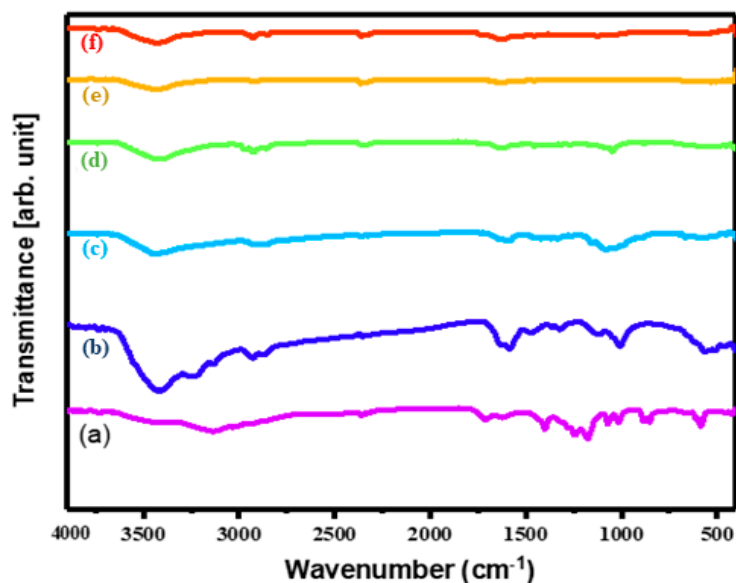


Figure 2. FTIR spectra of (a) CA, (b) CdS nanoparticles (NPs), (c) CdS CA 2% (d) CdS CA 4% (e) CdS CA 6%, and (f) CdS CA 8%.

In the Raman spectra of pristine CA, we observe two optical vibrational modes at around 1575 and 1375 cm^{-1} , which are ascribed to the G and D bands, respectively [34,37]. The CdS CA 8% sample also contains both G and D bands, which slightly moved to lower wavenumbers owing to the interaction between CA and CdS. In Figure 3b, there are two peaks at around 600 and 300 cm^{-1} due to the overtone (2-LO) and longitudinal optical photon mode (1-LO) of the CdS nanoparticles with CA [28,38,39]. Moreover, compared with the pure CA, a notable upsurge in the amplitude of the D and G bands is detected in the CdS CA 8% composite, which again shows the interaction between the CA and CdS.

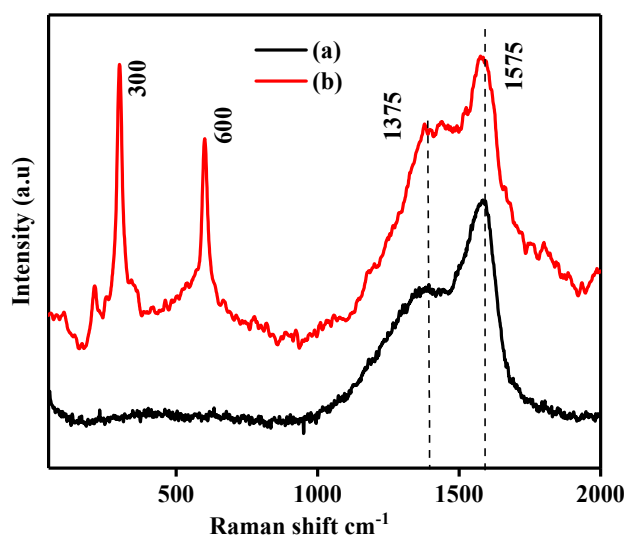


Figure 3. Raman spectra of (a) pristine CA and (b) CdS CA 8%.

The absorption of photons has a substantial role in the catalytic process. The photophysical properties of the as-prepared CdS and CdS–CA composites were studied by UV-vis analysis in the range of 200–800 nm, and the corresponding DRS spectra for a sequence of CdS CA nanocomposites are illustrated in Figure 4. The absorbance in the UV-vis region was increased in the composites containing CA in the CdS. These results clearly show that CA has a significant impact on CdS absorbance in the visible light ($\lambda \geq 400$ nm) region. Upsurge in absorption favors photocatalytic activity.

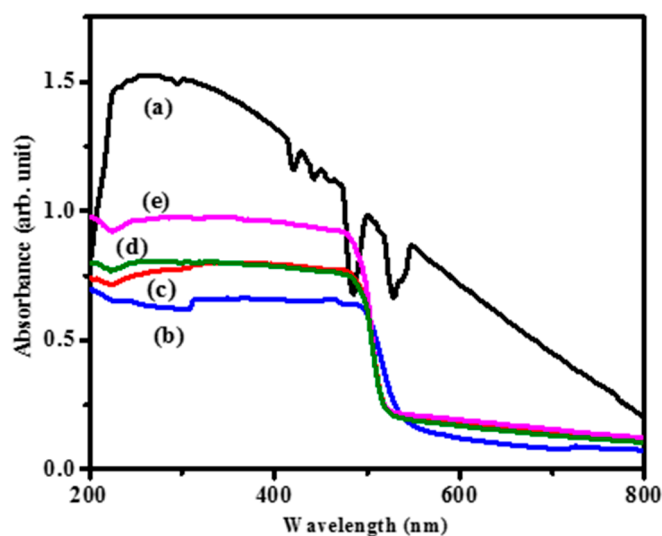


Figure 4. UV-DRS of (a) pure CA, (b) pristine CdS, (c) CdS CA 2%, (d) CdS CA 4% and (e) CdS CA 8%.

The UV spectra and band energy gap analysis of the materials are shown in Figure 5. Tauc's plots were used for prediction. The calculated band gap value of pristine CdS nanoparticles is 2.3, and the energy gap is 2.36 eV for CA-modified CdS nanocomposites. The band gap increased due to the blue shifted absorption. This narrow band gap offers outstanding channels for photocatalysis through the broader photoresponse range in the electromagnetic spectrum. The increased band gap may be attributed to two reasons: (i) the absorption influence from CA and (ii) the electrostatic charge transfer or interaction/binding between CA and CdS. An increased band gap energy within the visible region can increase the separation of h^+ and e^- and hinder the rapid recombination process of charge carriers.

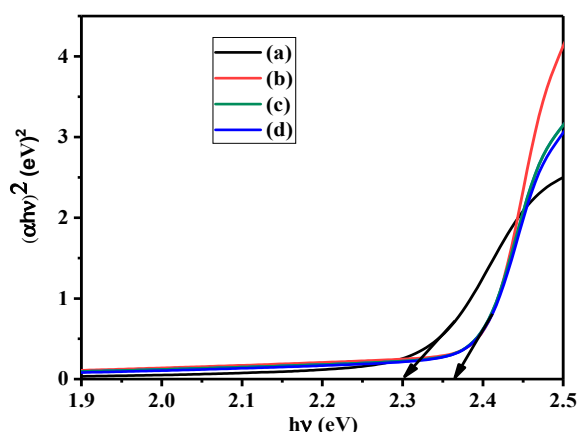


Figure 5. Tauc's plots for (a) pristine CdS, (b) CdS CA 2%, (c) CdS CA 4% and (d) CdS CA 8%.

The morphology of the as-prepared CA and CdS CA 8% NPs were examined by SEM analysis, and the corresponding images are shown in Figure 6. The SEM images of the CA shows a highly porous, 3D porous network with pore sizes in the range of some micrometers. Further, the SEM images of the sample show that the one-dimensional (1D) rods are bundles of nanorods that are oriented randomly. The nanorods have a diameter of approximately 60 nm and a length from 100 nm to approximately 2 μm , and they have a smooth surface along their entire length. Mapping analysis of the as-prepared CdS 8% CA NPs was performed by using the SEM images, and the analysis is shown in Figure S1. From the mapping analysis, the as-prepared CdS 8% CA NPs consisted of Cd, S, and C.

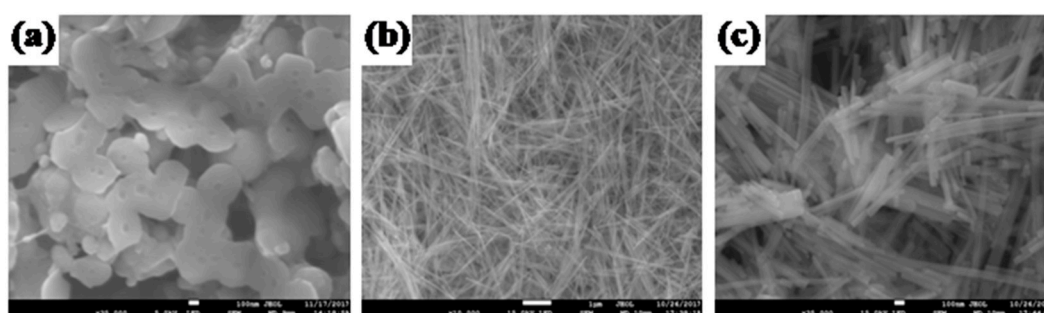


Figure 6. SEM pictures of (a) CA, (b) CdS CA 8% (low magnification), (c) CdS CA 8% (high magnification).

The TEM analysis of the synthesized samples was performed to further study the details of the morphology and microstructure of the CdS–CA 8% NPs (Figure 7). Figure 7b shows that the CdS–CA 8% NPs exhibited rod-like morphology, and the average size was 500 nm in length and approximately 100 nm in thickness. The dark black areas surrounded by gray represent carbon aerogel protected by rod-like CdS NPs. The SAED pattern of CdS CA 8% NPs indicates high crystallinity and agrees with the XRD analysis. Additionally, the TEM results are reliable with the SEM results.

The N_2 adsorption/desorption isotherms of CA and CdS CA 8% were examined by Brunauer–Emmett–Teller (BET) analysis and are shown in Figure 8. The result showed a BET surface of 27.67 m^2/g , Barrett, Joyner, and Halenda (BJH) collective surface area of 30.95 m^2/g , with BJH adsorption and desorption median pore diameter of 34.15 and 29.01 nm, respectively. The adsorption–desorption isotherm for CdS CA 8% displays typical Type IV properties and an H_2 -type hysteresis loop conferring to IUPAC classification, which is typical of mesoporous solids [40]. The presence of CA at a concentration of 8% in the CdS is revealed by the immediate increase in adsorption at relatively high pressure.

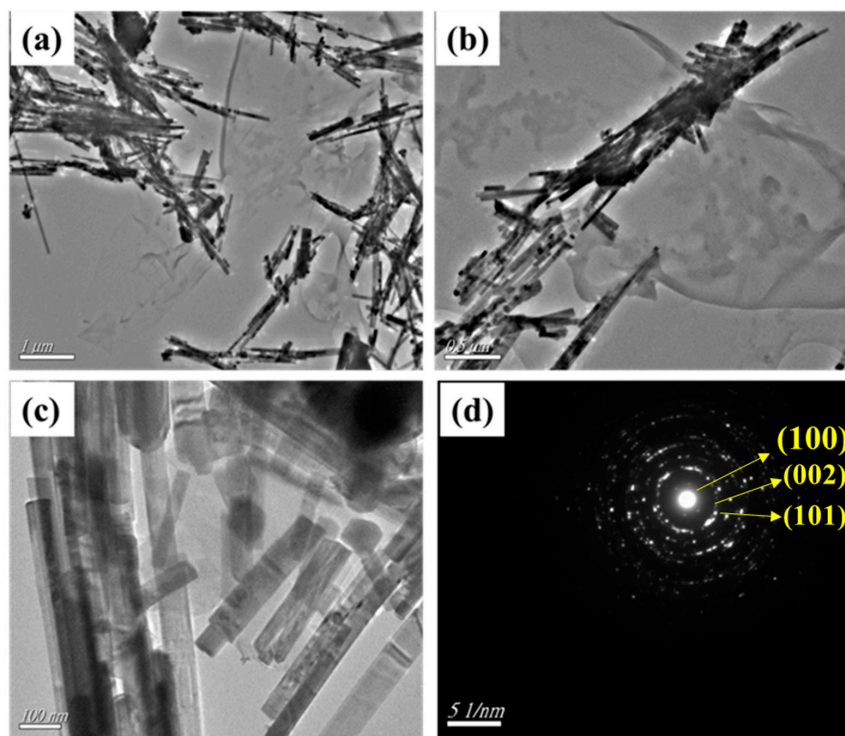


Figure 7. (a–c) TEM images and (d) SAED pattern of CdS CA 8% NPs.

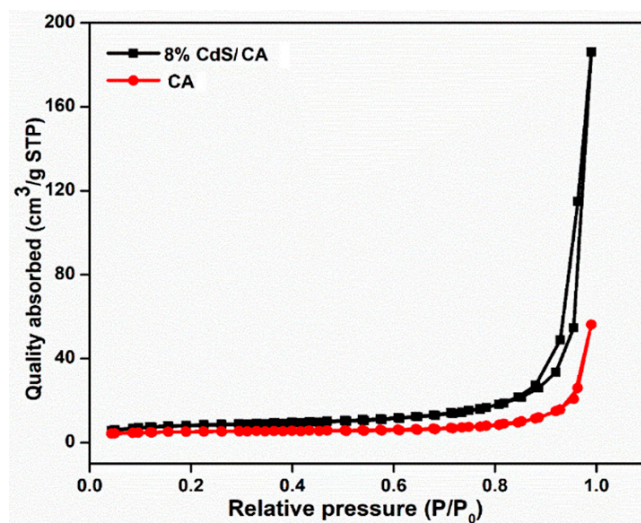


Figure 8. Nitrogen isotherms of the CA and CdS CA 8 wt% composites.

3.1. Photocatalytic Activity Evaluation of MB

MB dye was utilized to inspect the photocatalytic performance of the materials under VLI. The CdS CA 8% hybrid photocatalyst showed higher photocatalytic activities compared to the other samples, as depicted in Figure 9. After illumination, the absorption of MB in the visible spectral region (400–700 nm) was observably reduced. Furthermore, there were no peaks observed in the UV region for samples subjected to prolonged irradiation, which is most likely due to the disintegration of the aromatic structures as a whole.

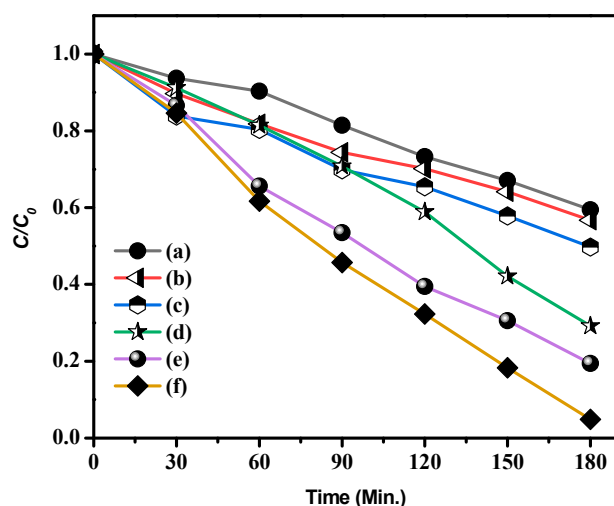


Figure 9. Photocatalytic degradation of methylene blue (MB) (a) CA, (b) CdS, (c) CdS CA 2% (d) CdS CA 4% (e) CdS CA 6% and (f) CdS CA 8%.

Figure S2 shows the light absorbance (UV-Vis) spectra of MB dye in the occurrence of catalyst at various time intervals. In these results, the pristine CdS NPs showed poor activity, in which approximately 43.27% of MB was decayed after VLI for 180 min. After combining the carbon aerogel with the CdS NPs, the experiments established that the CdS NPs with different percentages of added carbon aerogel were efficient visible light photocatalysts with higher performance than that of the CdS NPs. Notably, the photoactivity of 8% CA-added CdS NPs was around 2.19 times higher than that of CdS NPs, and this material had the best photoactivity. This result may be because combining carbon aerogel with CdS NPs can lead to the better splitting of e^-h^+ pairs (excitons), thus increasing the photocatalytic activity of the CdS NPs dramatically.

To clearly determine the kinetics of degradation of MB by the synthesized catalysts, the obtained experimental data were fitted with the pseudo-first-order model, $\ln(C_0/C) = kt$, where C_0 represents the initial conc., C signifies the conc. at time t , and k represents the first-order rate constant (Figure 10) [41].

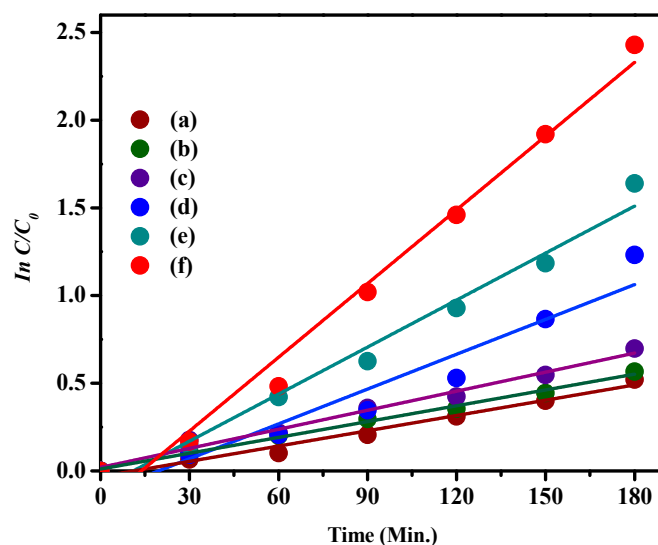


Figure 10. Pseudo-first-order kinetics fitting data for MB photodegradation by (a) CA, (b) CdS NPs, (c) CdS CA 2% (d) CdS CA 4% (e) CdS CA 6% and (f) CdS CA 8%.

All plots of $\ln(C_0/C)$ against time demonstrated a linear fit, and the slope of the linear regression is equal to the first-order apparent rate constant (K). The rate constant, degradation efficiency, and R^2 values are given in Table 1.

Table 1. Experiential pseudo-first-order rate constants (K_{app}), resultant correlation coefficients (R^2), and highest dye degradation (%) of the as-prepared nanoparticles.

Samples	K_{app} (min^{-1})	R^2	Maximum Dye Degradation (%)	Degradation Time (min.)
CA	0.0029	0.97654	40.57	180
CdS NPs	0.0036	0.98182	43.27	180
CdS 2% CA	0.0030	0.99318	50.24	180
CdS 4% CA	0.0066	0.91638	70.8	180
CdS 6% CA	0.0089	0.97728	80.57	180
CdS 8% CA	0.0140	0.98056	95.14	180

Figure 11 demonstrates the variation in the percent photodegradation with illumination time for the photodegradation of MB dye by the as-prepared samples. The synthesized CdS 8% CA sample showed a higher degradation efficiency (95.14%) for MB degradation than the bare CA (40.57%), CdS NPs (43.27%), CdS CA 2% (50.24%), CdS CA 4% (70.8%), and CdS CA 6% (80.57%) samples under the same conditions.

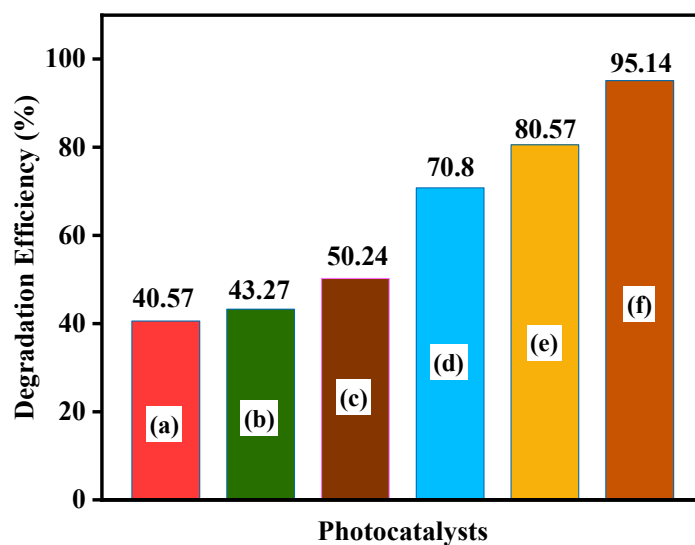


Figure 11. MB dye degradation efficiency of (a) CA, (b) CdS NPs, (c) CdS CA 2%, (d) CdS CA 4%, (e) CdS CA 6%, and (f) CdS CA 8%.

Stability and reusability are critical assessment parameters for the environmental friendliness of practical utilization. For each test, the photocatalysts were gathered, washed, centrifuged, dried, and recycled. Figure 12 shows five successive recycling experiments for photocatalytic degradation over CdS CA 8%. The slight catalyst deactivation may be accredited to the loss of material during the cycling runs. The photodegradation efficiency of CdS CA 8% still exceeded 89% after three cycles in comparison with the first cycle (95.14%).

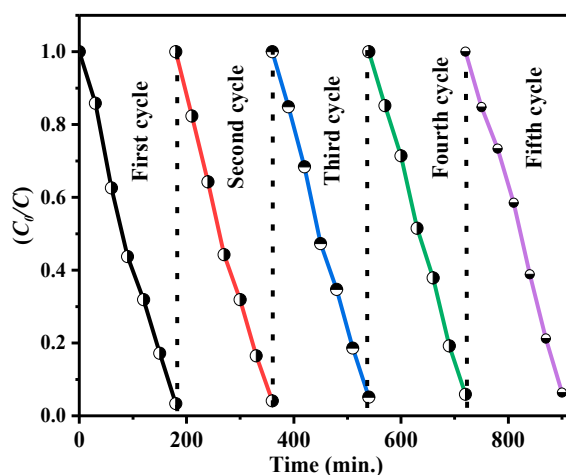


Figure 12. Cycling experiments for the degradation of MB by the as-prepared CdS CA 8% composite under visible light irradiation (VLI).

To analyze the function of these reactive species in the CdS CA 8% composite system, the effects of some radical scavengers on the photodegradation of MB were examined (Figure 13).

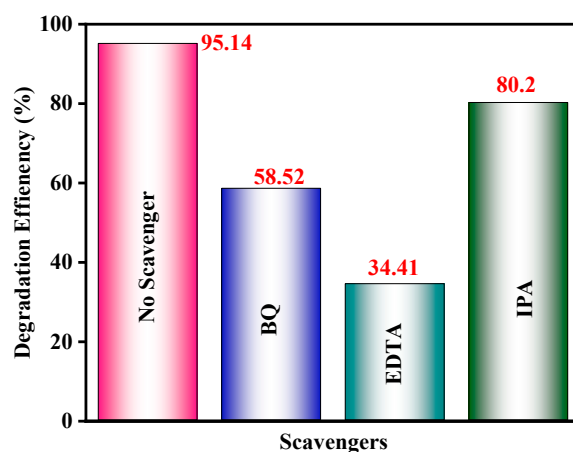


Figure 13. Effects of various scavengers on the degradation of MB in the presence of the CdS CA 8% photocatalyst under VLI.

The photodegradation processes of CdS–CA NPs without and with different sacrificial hole scavengers were studied in the 400–700 nm spectral range (visible light). The extraordinary transformation in photocatalytic performance is shown in Figure 12. The well-known $\bullet\text{O}_2^-$ scavenger benzoquinone (BQ) shows a moderate change in photocatalytic activity. However, 2-propanol (IPA), an $\bullet\text{OH}$ scavenger, retained 80.2% photocatalytic activity. This value is comparable with any other scavenger under analogous circumstances, demonstrating that holes and superoxide radicals $\bullet\text{O}_2^-$ are the chief reactive moieties in the CdS CA 8% photocatalyst.

3.2. Photocatalytic Activity Evaluation of Colorless Phenol

The photocatalytic response of the materials was assessed for the photodegradation of colorless phenol as a model pollutant under VLI, and the degradation results are shown in Figure 14. Removal efficiencies of 94.92%, 77.58%, 64.80%, 56.77%, 52.35%, and 39.29% were obtained using CdS CA 8%, CdS CA 6%, CdS CA 4%, CdS CA 2%, CdS NPs, and CA, respectively. Figure S3 shows the UV-Vis light absorbance of phenol in the occurrence of photocatalyst at various time intervals.

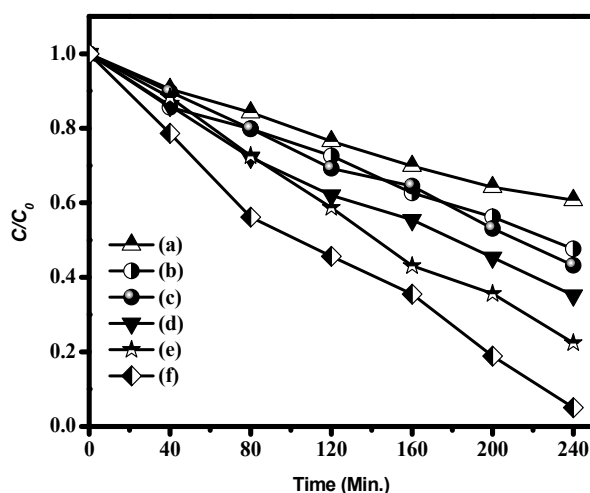


Figure 14. Photocatalytic phenol degradation by (a) CA, (b) CdS NPs, (c) CdS CA 2%, (d) CdS CA 4%, (e) CdS CA 6%, and (f) CdS CA 8%.

3.3. Photocatalytic Reaction Mechanism

The enhanced photocatalytic behaviour of the CdS as-prepared catalyst was extensively related to the photogenerated electron–hole pair. The proposed basic photocatalytic pathways (reaction mechanism) is given in Figure 15. In our case, the catalyst material absorbs the visible light energy equal or greater than that of the band energy gap and can generate an e^-h^+ (i.e., exciton) pair. The photoexcited e^- s move from the VB to the CB of CdS material; subsequently, unpaired h^+ is directly involved in the oxidation reaction. simultaneously, the photoexcited e^- are pumped to CA (function as e^- acceptor and donor medium); then, the e^- involves the redox reaction [42,43]. Here, the carbon aerogel act as a co-catalyst, which decreases the electron–hole pair recombination. To finish, the superoxide and hydroxyl radicals react with dye molecules and produce the by-products such as CO_2 , H_2O , etc.

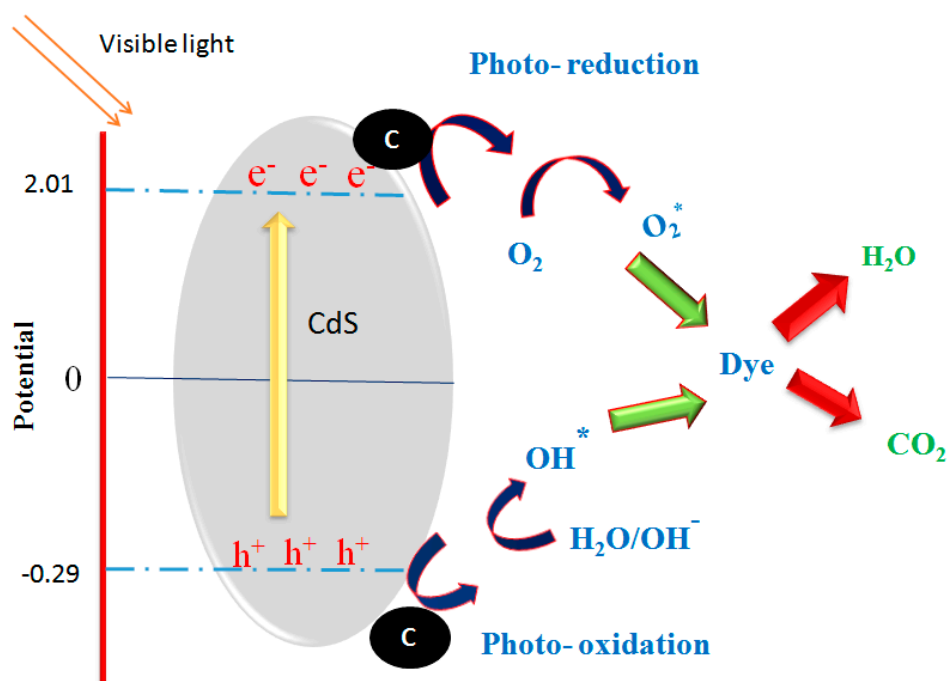


Figure 15. The schematic illustration of probable photodegradation mechanism over CdS–CA photocatalysts under visible light.

4. Conclusions

CA-assisted CdS nanorods were produced by a hydrothermal route and investigated as a photocatalyst for the degradation of MB dye and colorless phenol under VLI. The CA (8%)-assisted CdS nanoparticles show good photocatalytic activity toward MB dye; good stability is still shown after three cycles, and the activity exceeds 89% that of the first cycle. On the other hand, the photocatalytic activity changes substantially when adding holes and superoxide radicals, which demonstrates that holes and $\bullet\text{O}_2^-$ are the chief reactive moieties in the CdS CA 8% photocatalyst. The CdS CA 8% photocatalyst not only degrades dye but also degrades colorless phenol by nearly 94.92% within 240 min. From this investigation, we conclude that increasing the CA content in CdS nanorods also increases the photocatalytic activity through the enhanced UV-vis light absorption and large surface area.

Supplementary Materials: The following are available online at <http://www.mdpi.com/2073-4352/10/4/300/s1>, Figure S1: Elemental mapping image of CdS CA 8 wt% nanoparticles; Figure S2: UV-Visible absorption spectra of MB degradation of samples (a) CA, (b) CdS NPs, (c) CdS NC 2%, (d) CdS NC 4%, (e) CdS NC 6%, and (f) CdS 8%; Figure S3: UV-Visible absorption spectra of phenol degradation of samples (a) CA, (b) CdS NPs, (c) CdS CA 2%, (d) CdS CA 4%, (e) CdS CA 6%, and (f) CdS 8%.

Author Contributions: Conceptualization, S.P., K.B., and M.S.A.; T.A., G.P. and T.P.; investigation, formal analysis, M.J.A., T.P., K.B. and S.P.; resources, M.S.A.; methodology, P.S., G.P., T.P.; software, M.J.A., and S.P.; project administration, M.J.A.; validation T.A., G.P. and T.P.; writing—original draft preparation, S.P.; visualization, M.J.A., K.B. and S.P.; data curation, M.J.A.; supervision, M.S.A., and T.P.; writing—review and editing, M.S.A., T.A., G.P. and T.P. All authors have read and agreed to the published version of the manuscript.

Funding: King Saud University, Deanship of Scientific Research, Vice Deanship of Scientific Research Chairs, was the funder for this research work.

Acknowledgments: The authors are grateful to the Deanship of Scientific Research, King Saud University, for funding through the Vice Deanship of Scientific Research Chairs.

Conflicts of Interest: There is no conflict of interest to declare by authors.

References

- Shamsipur, M.; Rajabi, H.R. Study of photocatalytic activity of ZnS quantum dots as efficient nanoparticles for removal of methyl violet: Effect of ferric ion doping. *Spectrochim. Acta Part A Mol. Biomol. Spectrosc.* **2014**, *122*, 260–267. [CrossRef] [PubMed]
- Bhuvaneswari, K.; Bharathi, R.D.; Pazhanivel, T. Silk fibroin linked Zn/Cd-doped SnO₂ nanoparticles to purify the organically polluted water. *Mater. Res. Express* **2018**, *5*, 1–10. [CrossRef]
- Palanisamy, G.; Bhuvaneswari, K.; Bharathi, G.; Nataraj, D.; Pazhanivel, T. Enhanced Photocatalytic Properties of ZnS-WO₃ Nanosheet Hybrid under Visible Light Irradiation. *ChemistrySelect* **2018**, *3*, 9422–9430. [CrossRef]
- Yu, W.; Liu, X.; Pan, L.; Li, J.; Liu, J.; Zhang, J.; Li, P.; Chen, C.; Sun, Z. Enhanced visible light photocatalytic degradation of methylene blue by F-doped TiO₂. *Appl. Surf. Sci.* **2014**, *319*, 107–112. [CrossRef]
- Fang, J.; Fan, H.; Li, M.; Long, C. Nitrogen self-doped graphitic carbon nitride as efficient visible light photocatalyst for hydrogen evolution. *J. Mater. Chem. A* **2015**, *3*, 13819–13826. [CrossRef]
- Majeed, I.; Manzoor, U.; Kanodarwala, F.K.; Nadeem, M.A.; Nadeem, M.A.; Hussain, E.; Ali, H.; Badshah, A.; Stride, J.A. Pd-Ag decorated g-C₃N₄ as an efficient photocatalyst for hydrogen production from water under direct solar light irradiation. *Catal. Sci. Technol.* **2018**, *8*, 1183–1193. [CrossRef]
- Athanasidou, A.; Mitsionis, A.; Vaimakis, T.; Pomonis, P.; Petrakis, D.; Loukatzikou, L.; Todorova, N.; Trapalis, C.; Ladasc, S. A novel route for the production of TiO₂ photocatalysts with low energy gap, via Triton-X and oleic acid surfactants. *Appl. Surf. Sci.* **2014**, *319*, 143–150. [CrossRef]
- Zhao, Q.; Xie, Y.; Zhang, Z.; Bai, X. Size-selective synthesis of zinc sulfide hierarchical structures and their photocatalytic activity. *Cryst. Growth Des.* **2007**, *7*, 153–158. [CrossRef]
- Marci, G.; Augugliaro, V.; López-Muñoz, M.J.; Martín, C.; Palmisano, L.; Rives, V.; Schiavello, M.; Tilley, R.J.D.; Venezia, A.M. Preparation Characterization and Photocatalytic Activity of Polycrystalline ZnO/TiO₂ Systems. 1. Surface and Bulk Characterization. *J. Phys. Chem. B* **2001**, *105*, 1026–1032. [CrossRef]

10. Labiadh, H.; Hidouri, S. ZnS quantum dots and their derivatives: Overview on identity, synthesis and challenge into surface modifications for restricted applications ZnS quantum dots and their derivatives. *J. King Saud Univ. Sci.* **2017**, *29*, 444–450. [[CrossRef](#)]
11. Lei, R.; Zhang, H.; Ni, H.; Chen, R.; Gu, H.; Zhang, B. Novel ZnO nanoparticles modified WO₃ nanosheet arrays for enhanced photocatalytic properties under solar light illumination. *Appl. Surf. Sci.* **2019**, *463*, 363–373. [[CrossRef](#)]
12. Raza, W.; Faisal, S.M.; Owais, M.; Bahnemann, D.; Muneer, M. Facile fabrication of highly efficient modified ZnO photocatalyst with enhanced photocatalytic, antibacterial and anticancer activity. *RSC Adv.* **2016**, *6*, 78335–78350. [[CrossRef](#)]
13. Etacheri, V.; Di Valentin, C.; Schneider, J.; Bahnemann, D.; Pillai, S.C. Visible-light activation of TiO₂ photocatalysts: Advances in theory and experiments. *J. Photochem. Photobiol. C Photochem. Rev.* **2015**, *25*, 1–29. [[CrossRef](#)]
14. Hou, Y.; Yang, J.; Lei, C.; Yang, B.; Li, Z.; Xie, Y.; Zhang, X.; Lei, L.; Chen, J. Nitrogen Vacancy Structure Driven Photoelectrocatalytic Degradation of 4-Chlorophenol Using Porous Graphitic Carbon Nitride Nanosheets. *ACS Sustain. Chem. Eng.* **2018**, *6*, 6497–6506. [[CrossRef](#)]
15. Liu, T.; Cui, Z.W.; Zhou, J.; Wang, Y.; Zou, Z.G. Synthesis of pyridinic-rich N, S co-doped carbon quantum dots as effective enzyme mimics. *Nanoscale Res. Lett.* **2017**, *12*, 1–8. [[CrossRef](#)] [[PubMed](#)]
16. Micheal, K.; Ayeshamariam, A.; Devanesan, S.; Bhuvaneswari, K.; Pazhanivel, T.; AlSalhi, M.S.; Aljaafreh, M.J. Environmental friendly synthesis of carbon nanoplates supported ZnO nanorods for enhanced degradation of dyes and organic pollutants with visible light driven photocatalytic performance. *J. King Saud Univ. Sci.* **2020**, *32*, 1081–1087. [[CrossRef](#)]
17. Palanisamy, G.; Bhuvaneswari, K.; Pazhanivel, T.; Bharathi, G. Enriched photocatalytic activity of Rhodamine B dye from aqueous solution using hollow sphere tungsten trioxide nanoparticles. *Optik* **2020**, *204*, 164171. [[CrossRef](#)]
18. Huang, H.B.; Yu, K.; Wang, J.T.; Zhou, J.R.; Li, H.F.; Lü, J.; Cao, R. Controlled growth of ZnS/ZnO heterojunctions on porous biomass carbons: Via one-step carbothermal reduction enables visible-light-driven photocatalytic H₂ production. *Inorg. Chem. Front.* **2019**, *6*, 2035–2042. [[CrossRef](#)]
19. Wang, Q.; Lian, J.; Ma, Q.; Zhang, S.; He, J.; Zhong, J.; Li, J.; Huang, H.; Su, B. Preparation of carbon spheres supported CdS photocatalyst for enhancement its photocatalytic H₂ evolution. *Catal. Today* **2017**, *281*, 662–668. [[CrossRef](#)]
20. Li, Q.; Guo, B.; Yu, J.; Ran, J.; Zhang, B.; Yan, H.; Gong, J.R. Highly efficient visible-light-driven photocatalytic hydrogen production of CdS-cluster-decorated graphene nanosheets. *J. Am. Chem. Soc.* **2011**, *133*, 10878–10884. [[CrossRef](#)]
21. Cheng, L.; Xiang, Q.; Liao, Y.; Zhang, H. CdS-Based photocatalysts. *Energy Environ. Sci.* **2018**, *11*, 1362–1391. [[CrossRef](#)]
22. Yao, W.; Song, X.; Huang, C.; Xu, Q.; Wu, Q. Enhancing solar hydrogen production via modified photochemical treatment of Pt/CdS photocatalyst. *Catal. Today* **2013**, *199*, 42–47. [[CrossRef](#)]
23. Wu, W.; Liu, G.; Xie, Q.; Liang, S.; Zheng, H.; Yuan, R.; Su, W.; Wu, L. A simple and highly efficient route for the preparation of p-phenylenediamine by reducing 4-nitroaniline over commercial CdS visible light-driven photocatalyst in water. *Green Chem.* **2012**, *14*, 1705–1709. [[CrossRef](#)]
24. Li, W.; Feng, C.; Dai, S.; Yue, J.; Hua, F.; Hou, H. Fabrication of sulfur-doped g-C₃N₄/Au/CdS Z-scheme photocatalyst to improve the photocatalytic performance under visible light. *Appl. Catal. B Environ.* **2015**, *168–169*, 465–471. [[CrossRef](#)]
25. Shen, S.; Guo, L.; Chen, X.; Ren, F.; Mao, S.S. Effect of Ag₂S on solar-driven photocatalytic hydrogen evolution of nanostructured CdS. *Int. J. Hydrogen Energy* **2010**, *35*, 7110–7115. [[CrossRef](#)]
26. Li, Q.; Li, X.; Wageh, S.; Al-Ghamdi, A.A.; Yu, J. CdS/Graphene Nanocomposite Photocatalysts. *Adv. Energy Mater.* **2015**, *5*, 1–28.
27. Huang, H.B.; Wang, Y.; Cai, F.Y.; Jiao, W.B.; Zhang, N.; Liu, C.; Cao, H.L.; Lü, J. Photodegradation of rhodamine B over biomass-derived activated carbon supported CdS nanomaterials under visible irradiation. *Front. Chem.* **2017**, *5*, 1–10. [[CrossRef](#)]
28. Rodriguez, P.; Muñoz-Aguirre, N.; San-Martín Martínez, E.; González de la Cruz, G.; Tomas, S.A.; Zelaya Angel, O. Synthesis and spectral properties of starch capped CdS nanoparticles in aqueous solution. *J. Cryst. Growth* **2008**, *310*, 160–164. [[CrossRef](#)]

29. Li, X.; Yang, S.; Sun, J.; He, P.; Xu, X.; Ding, G. Tungsten oxide nanowire-reduced graphene oxide aerogel for high-efficiency visible light photocatalysis. *Carbon N. Y.* **2014**, *78*, 38–48. [\[CrossRef\]](#)
30. Jin, Y.; Wu, M.; Zhao, G.; Li, M. Photocatalysis-enhanced electrosorption process for degradation of high-concentration dye wastewater on TiO₂/carbon aerogel. *Chem. Eng. J.* **2011**, *168*, 1248–1255. [\[CrossRef\]](#)
31. Tong, H.; Zhu, Y.J. Synthesis of CdS nanocrystals based on low-temperature thermolysis of one single-source organometallic precursor. *Nanotechnology* **2006**, *17*, 845–851. [\[CrossRef\]](#)
32. Shanmugam, P.; Murthy, A.P.; Theerthagiri, J.; Wei, W.; Madhavan, J.; Kim, H.S.; Maiyalagan, T.; Xie, J. Robust bifunctional catalytic activities of N-doped carbon aerogel-nickel composites for electrocatalytic hydrogen evolution and hydrogenation of nitrocompounds. *Int. J. Hydrogen Energy* **2019**, *44*, 13334–13344. [\[CrossRef\]](#)
33. Wu, X.; Zhao, J.; Wang, L.; Han, M.; Zhang, M.; Wang, H.; Huang, H.; Liu, Y.; Kang, Z. Carbon dots as solid-state electron mediator for BiVO₄/CDs/CdS Z-scheme photocatalyst working under visible light. *Appl. Catal. B Environ.* **2017**, *206*, 501–509. [\[CrossRef\]](#)
34. Jiang, N.; Xiu, Z.; Xie, Z.; Li, H.; Zhao, G.; Wang, W.; Wu, Y.; Hao, X. Reduced graphene oxide-CdS nanocomposites with enhanced visible-light photoactivity synthesized using ionic-liquid precursors. *New J. Chem.* **2014**, *38*, 4312–4320. [\[CrossRef\]](#)
35. Wankhede, M.E.; Haram, S.K. Synthesis and characterization of CD-DMSO complex capped CdS nanoparticles. *Chem. Mater.* **2003**, *15*, 1296–1301. [\[CrossRef\]](#)
36. Xu, D.; Lei, F.; Chen, H.; Yin, L.; Shi, Y.; Xie, J. One-step hydrothermal synthesis and optical properties of self-quenching-resistant carbon dots towards fluorescent ink and as nanosensors for Fe³⁺ detection. *RSC Adv.* **2019**, *9*, 8290–8299. [\[CrossRef\]](#)
37. Qiu, B.; Xing, M.; Zhang, J. Mesoporous TiO₂ nanocrystals grown in situ on graphene aerogels for high photocatalysis and lithium-ion batteries. *J. Am. Chem. Soc.* **2014**, *136*, 5852–5855. [\[CrossRef\]](#)
38. Kumar, P.; Saxena, N.; Chandra, R.; Gaa, V.; Agarwal, A.; Kanjilal, D. Nanotwinning and structural phase transition in CdS quantum dots. *Nanoscale Res. Lett.* **2012**, *7*, 1–7. [\[CrossRef\]](#)
39. Jing, D.; Guo, L. A novel method for the preparation of a highly stable and active CdS photocatalyst with a special surface nanostructure. *J. Phys. Chem. B* **2006**, *110*, 11139–11145. [\[CrossRef\]](#)
40. Ouallal, H.; Dehmani, Y.; Moussout, H.; Messaoudi, L. Heliyon Kinetic, isotherm and mechanism investigations of the removal of phenols from water by raw and calcined clays. *Heliyon* **2019**, *5*, e01616. [\[CrossRef\]](#)
41. Teeparthi, S.R.; Awini, E.W.; Kumar, R. Dominating role of crystal structure over defect chemistry in black and white zirconia on visible light photocatalytic activity. *Sci. Rep.* **2018**, *8*, 1–11. [\[CrossRef\]](#) [\[PubMed\]](#)
42. Yao, C.; Yuan, A.; Wang, Z.; Lei, H.; Zhang, L.; Guo, L.; Dong, X. Amphiphilic two-dimensional graphitic carbon nitride nanosheets for visible-light-driven phase-boundary photocatalysis. *J. Mater. Chem. A* **2019**, *7*, 13071–13079. [\[CrossRef\]](#)
43. Yuan, A.; Lei, H.; Wang, Z.; Dong, X. Improved photocatalytic performance for selective oxidation of amines to imines on graphitic carbon nitride/bismuth tungstate heterojunctions. *J. Colloid Interface Sci.* **2020**, *560*, 40–49. [\[CrossRef\]](#) [\[PubMed\]](#)

